Development of a Viscous Cascade Code Based on Scalar Implicit Factorization

C. J. Knight* and D. Choi†
Avco Research Laboratory, Inc., Everett, Massachusetts

A viscous cascade code has been developed, first for two-dimensional configurations and then extended to three-dimensional linear cascades with flat, parallel endwalls. It employs scalar implicit approximate factorization, a finite-volume formulation, second-order upwind differencing, and a two-equation q-ω turbulence model based on integration to the wall. A special form of the thin-layer approximation for the compressible Navier-Stokes equations is used that gives accurate skin-friction predictions on highly skewed meshes, now based on sheared H-grids. The two-dimensional code has been validated by considering test cases for NASA energy efficient engine (E^3) blade and vane cascade geometries. The turbulence model displays proper boundary-layer transition behavior. The three-dimensional E^3 vane cascade also has been considered with straight endwalls. Agreement with experiment is quite good.

Introduction

RELIABLE numerical simulation of viscous flow in turbine cascades is a challenging undertaking. Cascade flowfields are typically transonic and quite complex, including passage and horseshoe vortices in three dimensions. Strong rotational effects and shocks also can be involved, the latter primarily for compressors, but these are not the focus in the present study. Highly skewed computational grids arise from the dual requirements of grid periodicity and large flow turning in high-performance cascade designs. This complicates the numerical formulation, particularly with regard to accurate skin-friction and heat-transfer prediction. Reynolds numbers are moderate, so boundary-layer transition is an essential part of the phenomenology. Finally, efficiency and robustness are key for a flow code to be incorporated into turbomachinery engineering design methodology.

This study describes development and preliminary validation of a thin-layer Navier-Stokes code based on scalar implicit approximate factorization[1] for steady cascade flowfields. The formulation is influenced by prior work of Coakley.[2,3] This particular approach was chosen because it can be fully vectorized[4] and because implicit methods provide good convergence characteristics on the highly refined grids needed to resolve the viscous sublayer. Integration to the wall was chosen as the safe alternative for complex three-dimensional flow and one that could later be used to assess wall function treatments. Theoretical studies[5,6] and recent experimental results[7] indicate there may be a logarithmic region in general. However, the gain in using wall functions may be more limited than in two-dimensional due to secondary flow. We plan to assess some of these issues now that the basic code capability is in hand.

A two-equation turbulence model was selected with a view to the future. A more fundamental approach is involved than in zero-equation models, particularly with regard to transition prediction in the presence of intense freestream turbulence.[8] This is a key consideration for heat-transfer prediction and also has impact on aerodynamic loss, as will be seen in the test cases. Effects of streamline curvature, as well as centrifugal and Coriolis forces in rotors are also essential ingredients. These have not yet been incorporated into the modeling. What has been addressed is the key numerical issue of properly handling turbulence source terms in the implicit update procedure, which are quite stiff in the vicinity of no-slip boundaries.

In what follows, the numerical formulation and modeling is first summarized before proceeding to preliminary code validation. Test cases are based on turbine cascade configurations developed under the NASA energy efficient engine (E^3) activity and studied experimentally by Kopper et al.[9] The basic algorithm and turbulence modeling are first assessed in two dimensions. This includes comparison to experiment at midspan for both laminar flow and a two-equation model. Then the code is extended to three-dimensional linear cascades, and the demanding vane cascade case is executed with straight endwalls. Comparisons with experiment illustrate the accuracy of the present method and its potential use as a viable aerodynamic design tool.

Flow Equations and Turbulence Model

The conservation law form of the compressible three-dimensional Navier-Stokes equations can be written in Cartesian coordinates as the vector relationship

$$\frac{\partial U}{\partial t}+\frac{\partial F}{\partial x}+\frac{\partial G}{\partial y}+\frac{\partial H}{\partial z}=0 \tag{1}$$

where (in transposed form)

$$U^T=(\rho,\ \rho u,\ \rho v,\ \rho w,\ E)$$

$$F^T=[\rho u,\ \rho u^2+p-\tau_{11},\ \rho uv-\tau_{21},\ \rho uw-\tau_{31},$$
$$(E+p)u-q_1-\tau_{11}u-\tau_{12}v-\tau_{13}w]$$

$$G^T=[\rho v,\ \rho uv-\tau_{12},\ \rho v^2+p-\tau_{22},\ \rho vw-\tau_{32},$$
$$(E+p)v-q_2-\tau_{21}u-\tau_{22}v-\tau_{23}w]$$

$$H^T=[\rho w,\ \rho uw-\tau_{13},\ \rho vw-\tau_{23},\ \rho w^2+p-\tau_{33},$$
$$(E+p)w-q_3-\tau_{31}u-\tau_{32}v-\tau_{33}w] \tag{2}$$

Only a perfect gas will be considered, in which case the static pressure and total energy per unit volume are

$$p=\rho RT$$

$$E=\frac{p}{\gamma-1}+\frac{\rho}{2}(u^2+v^2+w^2) \tag{3}$$

Presented as Paper 87-2150 at the AIAA/SAE/ASME/ASEE 23rd Joint Propulsion Conference, San Diego, CA, June 29-July 2, 1987; received Nov. 16, 1987.

*Director, Engine Technology. Member AIAA.
†Principal Research Scientist. Member AIAA.

The adiabatic index γ is assumed to be constant.

The shear stress tensor and heat flux vector components are most simply defined in Cartesian tensor notation. Linear forms for an isotropic medium will be employed, as

$$\tau_{ij} = \mu\left(\frac{\partial u_i}{\partial x_j} + \frac{\partial u_j}{\partial x_i}\right) + \lambda\frac{\partial u_k}{\partial x_k}\delta_{ij}$$

$$q_i = \kappa\frac{\partial T}{\partial x_i} \tag{4}$$

where $(x_1, x_2, x_3) = (x,y,z)$, etc., μ and λ are the two coefficients of viscosity, and κ is the thermal conductivity. Since an eddy viscosity formulation will be adopted, these relations apply to turbulent flow as well with suitable interpretation of μ, λ, and κ. Thus, $\mu = \mu_L + \mu_T$ with laminar viscosity given by Sutherland's law and eddy viscosity by a Kolmogorov relationship. The second coefficient of viscosity $\lambda = -\mu$ in the present code, recognizing that dilatational contributions are minor for transonic flows. Also, $\kappa = \mu_L/Pr + \mu_T/Pr_T$, where constant Prandtl numbers are assumed: $Pr = 0.72$ and $Pr_T = 0.9$.

Boundary-conforming, generalized coordinates underlie the computational formulation. Since the geometry for the three-dimensional test case involves parallel endwalls, it is adequate to restrict the coordinate transformation to $x(\xi,\eta)$ and $y(\xi,\eta)$, and the spanwise coordinate z is used directly. The strong conservation law form becomes

$$\frac{\partial U}{\partial t} + J\left(\frac{\partial \hat{F}}{\partial \xi} + \frac{\partial \hat{G}}{\partial \eta}\right) + \frac{\partial H}{\partial z} = 0$$

$$\hat{F} = F\frac{\partial y}{\partial \eta} - G\frac{\partial x}{\partial \eta}, \quad \hat{G} = G\frac{\partial x}{\partial \xi} - F\frac{\partial y}{\partial \xi} \tag{5}$$

for a time-independent grid, where $J = 1/(x_\xi y_\eta - x_\eta y_\xi)$ is the Jacobian determinant for the two-dimensional transformation $(x,y) \leftrightarrow (\xi,\eta)$. This specialized grid construction, involving stacking in the spanwise direction, reduces metric storage requirements and is easily generalized later. Cartesian velocity components are used as dependent variables.

Viscous terms in Eq. (5) are incorporated via a special form of the thin-layer approximation that has been found to maintain accuracy on highly skewed grids. It also involves a significant reduction in operation count compared to other treatments. Accuracy of this formulation was first checked by considering Mach 0.5 flow over an isolated flat plate with transverse gridlines inclined at an angle Θ. Laminar flow with viscosity proportional to temperature was assumed in order to directly compare with the Blasius solution. The relative change in skin friction was found to be 0.2% or less as Θ varied from 90 deg (orthogonal grid) to 10 deg, the usual extreme on a sheared grid for turbine inlet guide vanes. Shearing would be less severe on turbine blades. Later performance in the cascade code showed similar insensitivity to grid skewness.

Two-equation turbulence models appear to offer more long-term potential for cascade flows, particularly in the area of heat transfer prediction. Coakley's q-ω model was selected largely due to its numerical compatibility with asymptotic time integration procedures.[10] A drawback is that it is less tested than the older k-ϵ and k-ω^2 models, but then no turbulence model is well tested for cascade flow. The dependent variables are directly related to the turbulent kinetic energy k and dissipation rate ϵ via $q = \sqrt{k}$ and $\omega = \epsilon/k$; they define a turbulent velocity scale and inverse time scale, respectively. In terms of these variables, the eddy viscosity $\mu_T = \rho C_\mu D q^2/\omega$, where $C_\mu = 0.09$ and D is a near-wall damping function. In two dimensions,

$$D = 1 - \exp(-\alpha\rho q d_n/\mu_L) \tag{6}$$

was used for better robustness (compared to dependence on $\rho q^2/\omega\mu_L$), where d_n measures normal distance to the nearest airfoil and $\alpha = 0.0065$. This was generalized to three dimensions by redefining d_n as a Buleev length scale incorporating z.

The conservation law form of the q-ω model in Cartesian tensor notation is

$$\frac{\partial}{\partial t}(\rho q) + \frac{\partial}{\partial x_i}(\rho u_i q) = \frac{\partial}{\partial x_i}\left[\left(\mu_L + \frac{\mu_T}{Pr_q}\right)\frac{\partial q}{\partial x_i}\right] + \frac{\rho q}{2}\left(C_\mu D\frac{\mathbb{S}}{\omega} - \omega\right)$$

$$\frac{\partial}{\partial t}(\rho\omega) + \frac{\partial}{\partial x_i}(\rho u_i \omega) = \frac{\partial}{\partial x_i}\left[\left(\mu_L + \frac{\mu_T}{Pr_\omega}\right)\frac{\partial \omega}{\partial x_i}\right] + \rho\left(C_1 C_\mu \mathbb{S} - C_2\omega^2\right) \tag{7}$$

where $\mathbb{S} = (u_{i,j} + u_{j,i})u_{i,j}$ as used here. Flow dilatation has been dropped in both the turbulence source terms and the strain rate invariant $\mathbb{S}$ as negligible for transonic flow, after preliminary study. Turbulence constants used are those in Coakley's original publication: $C_1 = 0.045 + 0.405D$, $C_2 = 0.92$, $Pr_q = 1$, and $Pr_\omega = 1.3$, where C_μ and D are defined above. Making C_1 dependent on D is believed to be one reason that the q-ω model can be made relatively insensitive to time-step selection.

These relations assume the same basic form as Eq. (5) in curvilinear coordinates, with added source terms. The strain rate invariant is simplified through the thin-layer approximation using normal derivatives.

Numerical Method

The steady flow problem is solved using asymptotic time integration based on implicit methods. This involves iterative application of a linear relation of the form $L(\delta t)\cdot\delta U = \Delta U$ to convergence, where δU is the change in solution over time step δt, $\Delta U = -R^n\delta t$ measures the degree of unsteadiness, and R is the residual vector evaluated from steady flow terms in Eq. (5). A cell-based, finite-volume formulation is used in evaluating residuals. This allows greater flexibility in grid construction, and the code is set up with generalized data structures in mind for mixed grid topologies.[11] That entails use of pointer indices. Several component considerations are involved in implementation and will be discussed individually below.

Residual Evaluation

Accuracy of the discretization scheme is essential for reliable aerodynamic loss prediction. For example, advanced vane cascade designs can involve near 1% loss in stagnation pressure, which should ideally be estimated within 10–20% relative error (i.e., $1\text{–}2 \times 10^{-3}$ on $\Delta p_t/p_t$) for design purposes. That level of accuracy is difficult at transonic speeds. Two approaches were considered for evaluating residuals: upwinding and central differencing plus damping. In the latter case, both fourth-order and mixed second/fourth-order damping were evaluated and found inadequate on H-grids, due primarily to numerical instability encountered near leading and trailing edges. This might be circumvented using O-H grids. Second-order upwinding provided good code robustness even on H-grids and also improved accuracy.

The upwinding scheme uses Coakley's implicit, finite-volume formulation[3] with dissipation based on characteristic increments. It is adequate to consider one term in Eq. (5), say the ξ derivative. Let $\tilde{F}$ denote the transformed flux vector in the ξ direction and i denote the corresponding index at cell center. Other indices are suppressed for convenience. Then, discretization with $\delta\xi = 1$ involves $\partial\tilde{F}/\partial\xi \rightarrow \tilde{F}^*_{i+\frac{1}{2}} - \tilde{F}^*_{i-\frac{1}{2}}$ where the asterisks indicate numerical damping is added to assure near-monotone behavior; thus,

$$\tilde{F}^*_{i+\frac{1}{2}} = \tfrac{1}{2}(\tilde{F}_i + \tilde{F}_{i+1} - D_{i+\frac{1}{2}}) \tag{8}$$

It is important to base $\hat{F}^*_{i+\frac{1}{2}}$ on interpolation of flux vectors in order to get exact cancellation of the downwind contribution by the dissipation function $D_{i+\frac{1}{2}}$, especially near shock waves.

Similarity transformations arising from characteristics theory are used in evaluating the dissipation function. First, $\delta W_{i+\frac{1}{2}} = S_\xi \cdot (U_{i+1} - U_i)$ defines characteristic increments, where S_ξ is the matrix of left eigenvectors associated with the ξ direction. Then,

$$D_{i+\frac{1}{2}} = S_\xi^{-1} \cdot [|\Lambda_\xi|\delta W_{i+\frac{1}{2}} + \tfrac{1}{2}(\Lambda_\xi - |\Lambda_\xi|)\delta W_{i+3/2} - \tfrac{1}{2}(\Lambda_\xi + |\Lambda_\xi|)\delta W_{i-\frac{1}{2}}] \quad (9)$$

where Λ_ξ is a diagonal matrix of eigenvalues or characteristic directions associated with ξ. Elements of S_ξ and Λ_ξ are evaluated at the cell face $i + \frac{1}{2}$ using Roe averaging.[12] Similar expressions apply in the j and k directions. Third-order upwinding also could be implemented without major code changes but has not been tried yet.

Note that the level of damping is selective in the sense that it is different for each of the characteristic components. In particular, damping tends to zero for the tangential velocity components as a wall is approached, while remaining nonzero for acoustic components. Thus, there is reduced contamination of viscous predictions for a given level of smoothness in pressure variation normal to walls. This was established by comparison to conventional damping schemes in conjunction with central differencing, using C-grids at the time. Application of total variation diminishing (TVD) treatments has not been found necessary or particularly beneficial in work done thus far.

Scalar Factored Scheme

The scalar or diagonalized version of the approximate factorization algorithm is employed, a procedure best described in stages. Without viscosity, the Jacobians of the transformed flux vectors can be expressed as

$$A = S_\xi^{-1}\Lambda_\xi S_\xi, \qquad B = S_\eta^{-1}\Lambda_\eta S_\eta, \qquad C = S_z^{-1}\Lambda_z S_z \quad (10)$$

where S is a matrix of left eigenvectors, Λ a diagonal matrix of eigenvalues, and subscripts denote the respective directions. Using these and making a weak wave approximation, the general algorithm can be manipulated to find

$$(I + J\delta t \frac{\partial}{\partial \xi}\Lambda_\xi) \cdot S_\xi \delta U^* = S_\xi \cdot \Delta U$$

$$(I + J\delta t \frac{\partial}{\partial \eta}\Lambda_\eta) \cdot S_\eta \delta U^{**} = S_\eta \cdot \delta U^*$$

$$(I + J\delta t \frac{\partial}{\partial z}\Lambda_z) \cdot S_z \delta U = S_z \cdot \delta U^{**} \quad (11)$$

where $\delta U = U^{n+1} - U^n$ is the overall change during the time step and ΔU measures the degree of unsteadiness as explained at the beginning of this section.

Since the Λ matrices are diagonal, Eq. (11) consists of a sequence of linear transformations and scalar algebraic relations. The net result is significantly fewer operations than for a block implicit scheme, and the reduced storage requirements allow Gaussian eliminations to be fully vectorized.[4] Further economy results by factoring the eigenvector matrices into their component parts.[2] The important point is that the component transformations contain many zeros, allowing multiplication by such elements to be excluded in the coding.

The Jacobians associated with the viscous terms are not diagonalized by the inviscid similarity transformations. This necessitates using an ad hoc procedure. The approach adopted consists of adding a second derivative times the maximum eigenvalue of the viscous Jacobian for each of the transverse directions in Eq. (11). Central differencing is used for these viscous contributions; and first-order upwinding was found adequate for left-side convection terms when second order upwinding is used for residuals. This assures diagonal dominance of the coefficient matrices, provides acceptable convergence, and reduces update cost somewhat by allowing a switch to tridiagonal solvers. Accuracy of the steady-state solution is not affected.

Ad hoc incorporation of turbulence source terms into the implicit coefficient matrix, as originally suggested by Coakley,[10] was found less than ideal. This was replaced by a suitable scalar approximation to the Jacobian of the turbulence source terms, considering only the dissipative contributions as suggested by Viegas.[13] After experimentation, it was determined that this treatment is best incorporated as a postprocessing step. Thus,

$$\delta q = \delta q^*/(1 + 2C_2\omega^*\delta t)$$

$$\delta \omega = \delta \omega^*/(1 + 2C_2\omega^*\delta t) \quad (12)$$

where $\omega^* = \omega^n + \delta\omega^*$, asterisks denote provisional values given by the augmented version of Eq. (11), and $C_2 = 0.92$. The effect of the denominator is to limit excursions in turbulence quantities after a sudden start, particularly near no-slip boundaries.

Boundary Treatment

Careful boundary treatment is essential to good implicit code performance. An immediate issue is how to implement a fully implicit formulation, which involves several considerations. Similarity transformations underlying the scalar factored scheme generally do not uncouple characteristic variables at the boundary. For example, the two acoustic components are related by the requirements of no throughflow at an impermeable wall. Linear superposition is used to maintain the basic scalar philosophy in Eq. (11), while rigorously imposing proper cross-coupling at boundaries. Extraneous boundary conditions also arise; for example, determination of static pressure on walls. These are handled by using a first-order accurate treatment for implicit update and then correcting results explicitly afterward to assure full second-order spatial accuracy. This essentially eliminates time-step restrictions associated with boundary treatment and maintains simplicity.

Several types of boundaries are involved in the cascade flow problem. At the inflow plane, the flow angle, stagnation temperature, and stagnation pressure are specified. The first two conditions imply a relationship between acoustic components during update, the latter defines the entropy increment in terms of the incoming pressure pulse, and transverse velocity increments are related to the change in total velocity through the flow angle. The required additional condition is obtained by extrapolating the left-running Riemann increment, i.e., $\delta Q_1 = \delta Q_2$. Turbulence quantities also must be specified. Constant values are used in two dimensions, but the endwall boundary layer must be considered in three dimensions. This involves an equilibrium assumption for ω and determination of q such that the eddy viscosity is the same as given by the Cebeci-Smith model.[14] The inflow velocity is assumed to consist of constant velocity in the core flow region and an endwall boundary layer described by a power law profile plus a straight-line segment over the viscous sublayer. Stagnation pressure also is adjusted in accordance with that profile for three dimensions.

Static pressure is specified at the outflow plane in the current code. This might have to be re-examined for more extreme supercritical situations than in the test cases but performs adequately for present purposes. This implies a relationship between Riemann increments (i.e., $\delta P_N = \delta Q_N$), and all other variables are treated by first-order extrapolation during implicit update. This is subsequently corrected to sec-

ond-order extrapolation based on upwind differencing. The solution domain is extended beyond the experimental "exit plane" in order to minimize possible contamination of wake decay characteristics.

Solid boundaries on the airfoil surface and endwall involve $u = v = w = 0$ and either an adiabatic or isothermal boundary condition. Acoustic extrapolation from the interior is used during implicit update, a procedure that gives a considerable acoustic pulse for a sudden start. Nevertheless, no problems with numerical stability were encountered. Only $\partial T/\partial n = 0$ is considered in the test cases. This implies a relationship for the entropy increment in terms of the pressure pulse. Boundary conditions on turbulence quantities entail $q = \partial\omega/\partial n = 0$. Reflected points are used in the grid construction so that normal derivative conditions are imposed with second order accuracy on the wall, which lies on cell faces.

Early experience showed that periodicity must be strictly imposed during implicit update; otherwise, severe instability can arise. This is greatly facilitated by using periodic grids in the blade-to-blade direction so that each η gridline can be considered individually. With $j = 1$ and $j = N$ on reflected gridlines and other indices suppressed for convenience, periodicity requires $\delta P_1 = \delta P_{N-1}$, $\delta P_2 = \delta P_N$, and similarly for other characteristic increments. The coefficient matrix is no longer tridiagonal, but generalization of the usual Gaussian elimination algorithm provides a solution with few added operations.

The three-dimensional test case involves symmetry across midspan, where $w = 0$. The other condition was provided by acoustic extrapolation rather than using strict symmetry. No stability problems arose in this case. Other variables were treated by assuming zero spanwise gradient. Strict symmetry was imposed subsequent to the implicit update procedure, with cell faces on the midplane.

Local Time-Step Selection

Experience has shown that more rapid convergence to a steady-state solution is obtained by using a local time step that is spatially varying. Dual time-step selection criteria are employed in the viscous cascade code. In the inviscid core region, it is reasonable to base the selection on the Courant-Friedricks-Levy (CFL) condition for one-dimensional wave propagation in the three coordinate directions:

$$\delta t_\xi \to \frac{1}{J}\left[\left|u\frac{\partial y}{\partial \eta} - v\frac{\partial x}{\partial \eta}\right| + a\sqrt{\left(\frac{\partial x}{\partial \eta}\right)^2 + \left(\frac{\partial y}{\partial \eta}\right)^2}\right]$$

$$\delta t_\eta \to \frac{1}{J}\left[\left|v\frac{\partial x}{\partial \xi} - u\frac{\partial y}{\partial \xi}\right| + a\sqrt{\left(\frac{\partial x}{\partial \xi}\right)^2 + \left(\frac{\partial y}{\partial \xi}\right)^2}\right]$$

$$\delta t_z = \delta z/(|w| + a) \tag{13}$$

where $J = 1/(x_\xi y_\eta - x_\eta y_\xi)$, a is the local sound speed, and suitable finite differencing is implied in the first two cases. The value of δt_{CFL} is then chosen as the CFL number times the minimum of δt_ξ, δt_η, and δt_z. There is an optimum value of CFL for rapid convergence, generally in the range of 3–5.

The drawback to using δt_{CFL} everywhere is that it gives slow entropy wave clearing in refined grid regions. Thus, final time-step selection is based on

$$\delta t = \max\,(\delta t_{\mathrm{CFL}}, \delta t_{\min}) \tag{14}$$

where δt_{CFL} is defined above and $\delta t_{\min}$ allows substantially increased CFL number in viscous dominated regions. Study in two dimensions led to $\delta t_{\min} = \delta t_\xi$, a compromise between rapid entropy clearing and reduced convergence due to splitting error. This choice was particularly significant in the wake region. Splitting errors in corner regions led to a modified choice in three dimensions for a stacked, sheared grid,

$$\delta t_{\min} = \delta t_\xi \cdot \max\left(\frac{\delta z}{\delta z_{\max}}, \frac{\delta y}{\delta y_{\max}}\right) \tag{15}$$

where δy and δz are increments in Cartesian coordinates across a cell in pitchwise and spanwise directions, respectively, and the corresponding maximum values are specified by the user for grid construction. Equation (15) tends to reduce to the two-dimensional form well away from corners.

Two-Dimensional Computational Results

Turbulence modeling was first validated by considering an isolated flat plate at zero angle of attack. Early work considered two versions of the q-ω model defined by Coakley,[10] one with the turbulence damping function defined as in Eq. (6) and the other with D expressed in terms of the turbulent Reynolds number $\rho q^2/\omega\mu_L$. The second version was not reliable in properly predicting turbulent flow well downstream of a sharp leading edge; instead, the flow remained laminar when uniform flow properties were assumed initially. Further study showed that a good initial guess for q and ω is required for a flat plate to assure proper convergence using damping based on $\rho q^2/\omega\mu_L$. These difficulties were eliminated by switching to the first version, even when constant turbulence quantities were assumed everywhere initially. All discussion hereafter involves use of Eq. (6).

Skin-friction variation along the flat plate is shown in Fig. 1, together with expected laminar and turbulent behavior for comparison. The q-ω model displays at least rudimentary capability to predict laminar to turbulent transition, beginning at $Re_x = 1.7 \times 10^5$. This is a reasonable possibility when transition is dominated by diffusion of freestream turbulence through the boundary layer.[8] Quantitative comparison of the q-ω model to experiment has not yet been pursued for the intense turbulence characteristic of turbomachinery. Results in Fig. 1 are for inflow freestream quantities $q_\infty/U_\infty = 0.02$ and $\omega_\infty L/a_0 = 0.17$, where U_∞ is the freestream speed, L the plate chord length, and a_0 the stagnation sound speed.

Figure 2 shows velocity defect decay for a flat plate with $M_\infty = 0.5$ and $Re_L = 1 \times 10^6$. Distance downstream in the wake is normalized by the boundary-layer thickness Θ at the trailing edge. Predicted behavior is in good agreement with experimental data of Ramaprian et al.[15] Vandrome has done computations for this case using both the k-ϵ and k-ω^2 model, which are quite similar.[16] This, together with studies of the boundary-layer region, represents an essential demonstration of the validity of the viscous flow formulation. As long as the flow is attached or weakly separated, we have a reasonable degree of confidence in the two-dimensional modeling.

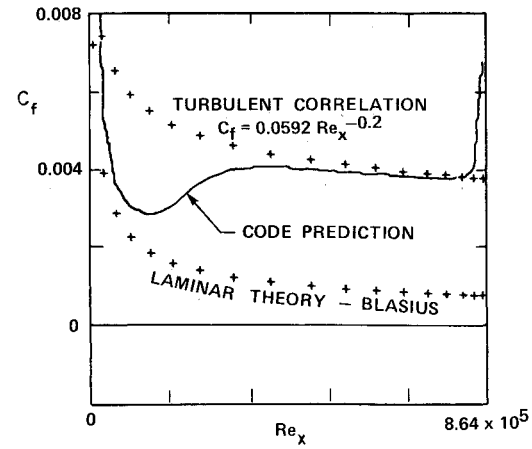

Fig. 1 Skin friction variation along flat plate ($M_\infty = 0.5$, $Re_L = 1 \times 10^6$).

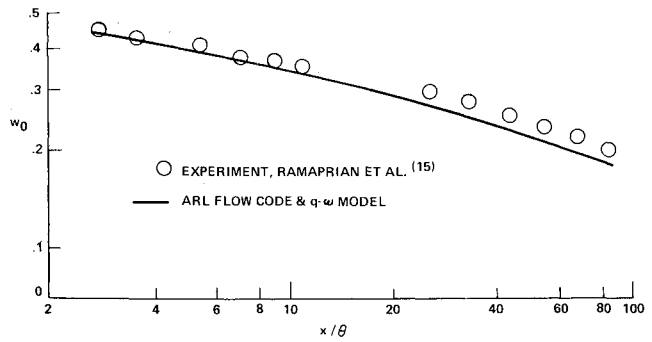

Fig. 2 Turbulent wake defect after a flat plate ($M_\infty = 0.5$, $Re_L = 1 \times 10^6$).

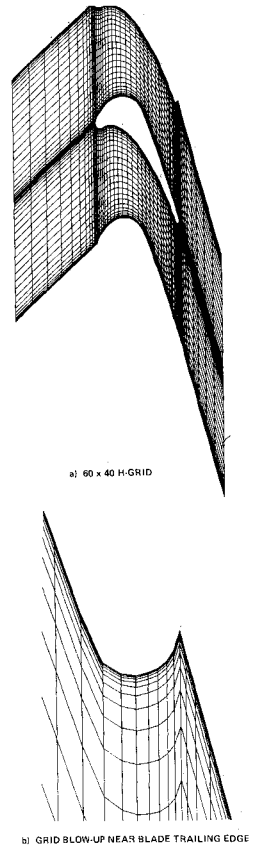

Fig. 3 H-grid for NASA E³ blade case (60 × 40 points).

The two-dimensional viscous cascade code is referred to as HCAS2D, the first letter indicating that it uses an H-grid. A typical example is shown in Fig. 3 for the NASA E³ rotor blade configuration considered by Kopper et al.[9] This 60 × 40 grid is constructed algebraically using a scheme that has specified normal spacing for the first cell off the wall, an exponentially expanding mesh over the inner part of the boundary layer, and a smooth blending into uniform spacing over the inviscid core region. In this case, $\delta n_{\min}/c_x = 5 \times 10^{-5}$ was used to property resolve the viscous sublayer, where c_x is the axial chord length. Note that the mesh wraps around the airfoil much as an 0-grid would, as seen in Fig. 3b. The minimum axial grid spacing near the leading edge is 0.01 c_x, and 0.003 c_x is used near the trailing edge; the respective radii are 0.066 and 0.023 c_x.

The E³ blade was designed to achieve a high velocity ratio across the rotor in a single-stage turbine. A representative case was considered in which flow enters at Mach 0.25 with a 43 deg angle and exits at an average Mach number of 1.04 with a 15.3 deg angle. Only the inlet angle was set in the code. The

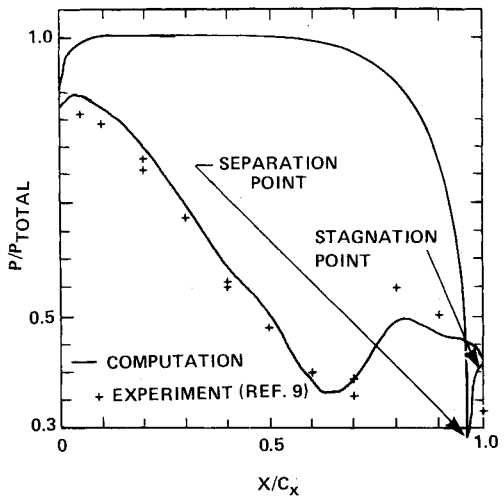

a) q-ω turbulence model

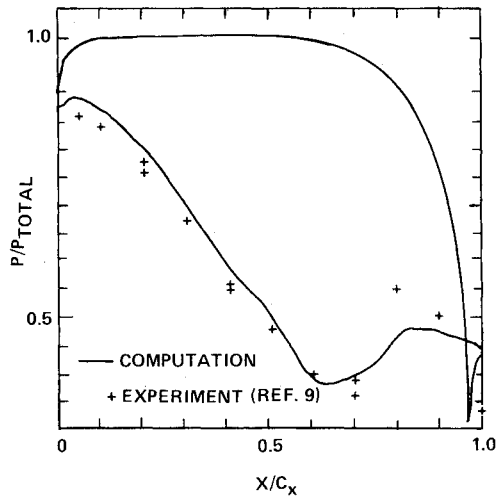

b) Laminar case

Fig. 4 Airfoil surface pressure distribution for E³ blade ($M_e = 1.1$).

isentropic exit Mach number $M_e = 1.1$, corresponding to an isentropic expansion ratio of 0.468 at the exit plane. This is below the design point at $M_e = 1.27$. Since significant aerodynamic loss occurs with the flow turning involved (122 deg), this is a relatively easy case by computational standards. That is the main reason a coarse viscous grid can be employed. The Reynolds number is 5.0×10^5 based on exit conditions and axial chord. Inlet freestream turbulence quantities $q_\infty/a_0 = 0.0036$ and $\omega c_x/a_0 = 0.12$ were assumed, where a_0 is the plenum sound speed. No information on these was provided by the experimentalists.

Figure 4 shows the predicted pressure on the cascade surface as compared with experimental data. Note that the turbulent solution shows somewhat stiffer pressure recovery than the laminar case. This is caused by altered boundary-layer growth on the suction surface just downstream of the throat due to transition. The overall comparison is very good. Some discrepancy along the early part of suction surface is presumably due to the H-grid structure near the leading edge. Two pressure dips near the pressure side trailing edge can be explained from a velocity vector plot shown in Fig. 5. We can easily find the stagnation point and the separation point. These two points correspond to the pressure extreme noted in Fig. 4. This illustrates that the thin-layer code with an H-grid topology can plausibly handle complicated recirculating flows near the blunt trailing edge. Unfortunately, there are no experimental

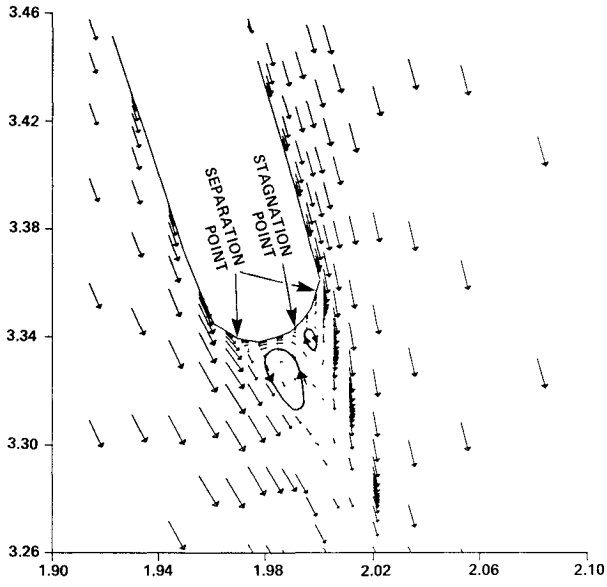

Fig. 5 Velocity-vector plot near blade trailing edge.

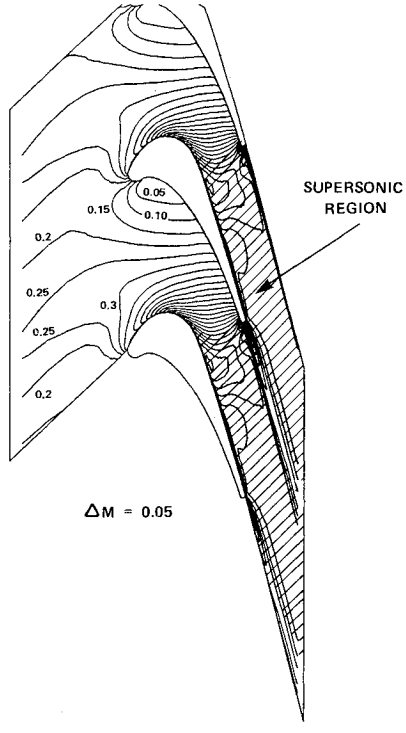

Fig. 6 Mach number contours for E^3 blade case.

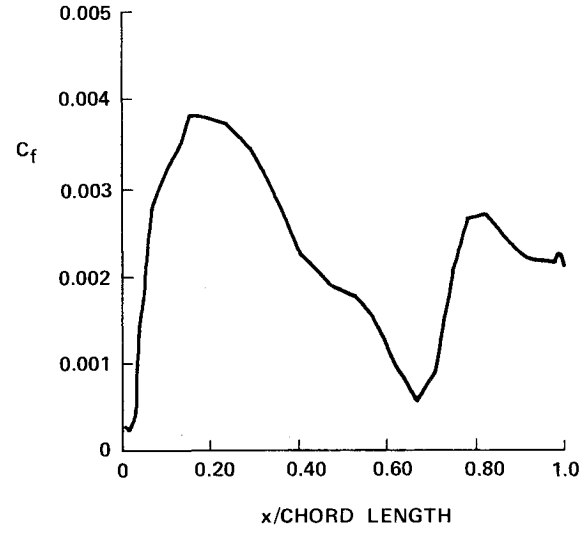

a) q-ω turbulence model

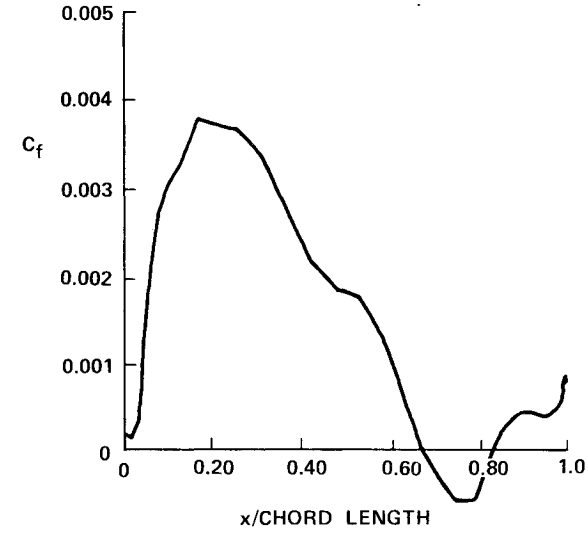

b) Laminar case

Fig. 7 Skin friction coefficient on E^3 blade suction surface.

data available to compare with this detailed predicted flow structure.

Mach contours in Fig. 6 give an overall picture of flowfield development for a stationary cascade. The flow accelerates from Mach 0.25 at the inlet to a peak Mach number of 1.25 on the suction surface near the throat and exits downstream at near sonic conditions. Figure 7 shows axial variation of skin friction coefficient on the suction surface, with local freestream dynamic head estimated from wall pressure and isentropic relations. By comparing results for laminar flow and the q-ω model, transition is seen to occur between 70 and 80% chord in the latter case. This is roughly in accord with experimental observations. It is also interesting to note that a laminar boundary layer would undergo substantial separation. From Fig. 6, flow deceleration downstream of the throat on the suction surface is implicated as an underlying factor triggering transition. Flow remains laminar on the pressure surface in code results as in the experiment.

The predicted exit flow conditions are compared with experimental data in Table 1 for the baseline cascade geometry. The experimental flow angle is believed to be closer to 17 deg according to Kopper et al.,[9] based on continuity checks and measured airfoil loadings; thus, agreement with mass-average angle from the code is likely to be better than indicated. Loss estimates also agree reasonably well with experiment even on the coarse grid used, presumably because viscous losses are substantial for the rotor cascade and hence dominate numerical error. The error is estimated to be about 1%. Axial variation of total pressure loss is shown in Fig. 8. Note that transition has significant influence on loss, as does base drag on the blunt trailing edge. One reason for selecting the case considered was that the base pressure coefficient reached a minimum at $M_e = 1.1$ in the experiment.

A second, more demanding test case has been considered in greater detail. The E^3 vane configuration is typical of advanced turbine inlet nozzle designs, involving rapid flow acceleration and relatively low stagnation pressure loss. The geometry is described in detail in Ref. 9. For this case, the flow enters at zero angle of incidence at low subsonic Mach number

Table 1 Comparison of predicted exit flow condition to experiment for E^3 rotor on 60 × 40 grid

Condition	Experiment	Computation	
		Laminar	Turbulent
M_e	1.1	1.1	1.1
Area-averaged Mach no.	1.044 ± 0.01	1.06	1.05
Mass-averaged $\Delta p_t/p_t$	0.0463 ± 0.01	0.0423	0.0567
Exit flow angle, deg	15.3 ± 2.5	16.5	16.81

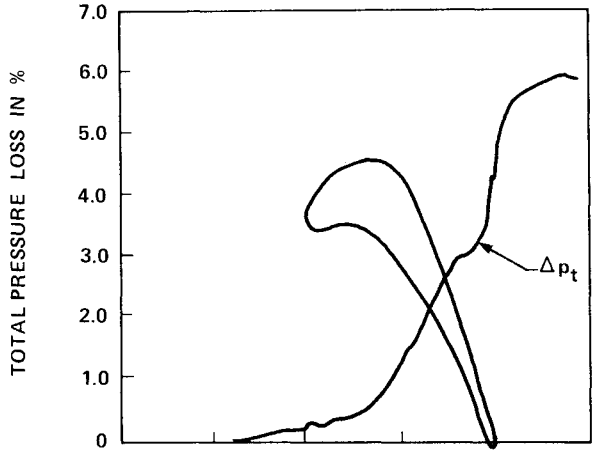

a) q-ω turbulence model

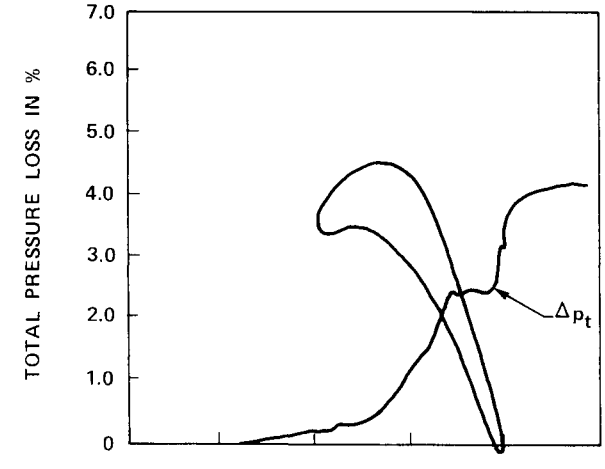

b) Laminar flow

Fig. 8 Axial variation of predicted pressure loss on 60 × 40 grid.

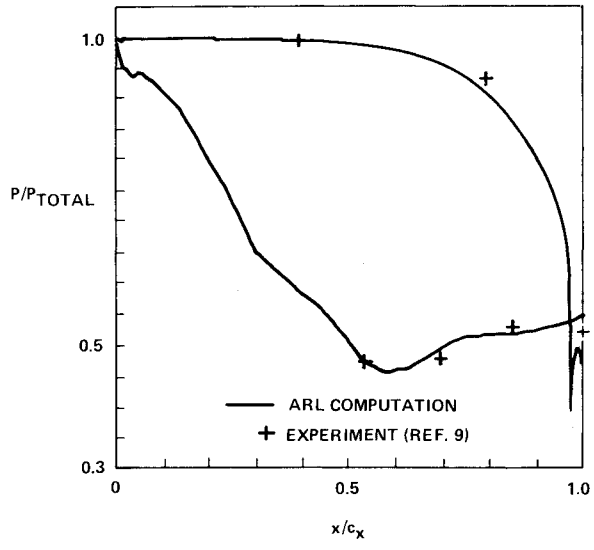

a) q-ω turbulence model

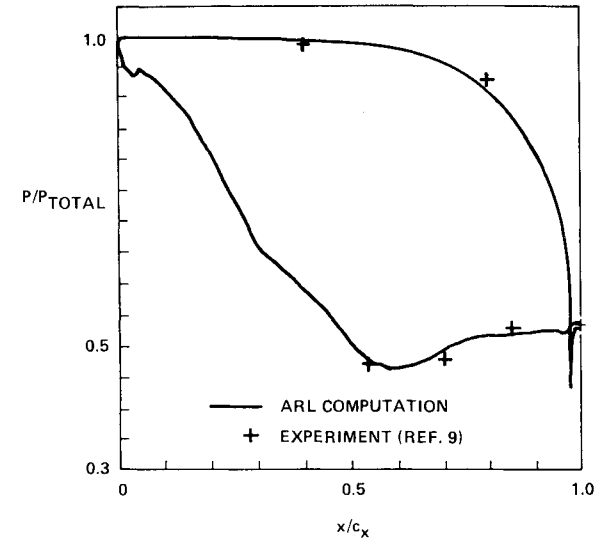

b) Laminar case

Fig. 9 Airfoil surface pressure distribution for E^3 vane (M_e = 1.0).

and exits near sonic conditions. Total flow turning is close to 80 deg. A 133 × 50 H-grid system was used for good accuracy. The minimum axial grid spacing near the leading edge was 0.01 c_x, and the grid spacing near the trailing edge was chosen based on 10 deg angular increments to adequately describe the circular shape of the trailing edge. Respective radii are 0.157 and 0.016 c_x. Correct description of the blunt trailing edge is very important to predict detailed flowfields there. The normal distance for the first grid point from the nonslip wall was chosen as $\delta n_{\min}/c_x = 1 \times 10^{-4}$, well within the viscous sublayer. The Reynolds number is 6.4×10^5 based on exit conditions and axial chord, and the inlet turbulence quantities are the same as for the rotor case.

Results are first given for $M_e = 1.0$, corresponding to an isentropic expansion ratio of 0.528. Predicted surface pressure is compared to experimental data in Fig. 9 with good agreement. Note that laminar and turbulent results are quite similar, in contrast to Fig. 4. Mach contours in Fig. 10 display the rapid expansion involved in this vane design. Flow accelerates from $M \sim 0.1$ to mildly supersonic conditions on the suction surface just downstream of the throat and then decelerates to near sonic conditions at the exit. Figure 11 shows variation in skin friction on the suction surface based on laminar flow and the q-ω model. By comparing these, we can easily locate transition behavior at 60–70% chord, as observed in the experiment. Flow remained laminar on the pressure surface. This shows again that the q-ω model is promising. Unfortunately, there is no comparable quantitative experimental skin-friction data. Heat-transfer data are another possibility that has not been explored thus far.

Predicted exit flow conditions are compared with experimental data for two grids in Table 2. The first is a coarse grid used in exploratory studies, and the second is the grid used in generating results above, with both linear cell dimensions reduced a factor of two in the inviscid core. Each grid involves about 15 points across both the suction and pressure surface boundary layers. The main quantity that shows grid dependence is stagnation pressure loss. Comparison indicates that

Table 2 Comparison of predicted exit flow condition to experiment for E^3 stator and two grids

		Computation			
		Laminar		Turbulent	
Condition	Experiment	70 × 40	133 × 50	70 × 40	133 × 50
M_e	1.0	1.0	1.0	1.0	1.0
Area-averaged Mach no.	0.974 ± 0.02	0.96	0.978	0.94	0.967
Mass-averaged $\Delta p_t/p_t$	0.02 ± 0.0016	0.039	0.019	0.064	0.034
Exit flow angle, deg	10.6 ± 0.4	10.95	10.7	11.31	10.91

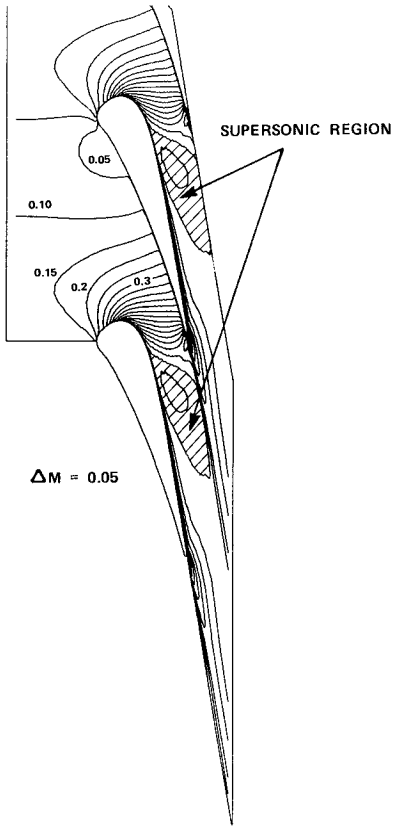

Fig. 10 Mach number contours for E^3 vane case.

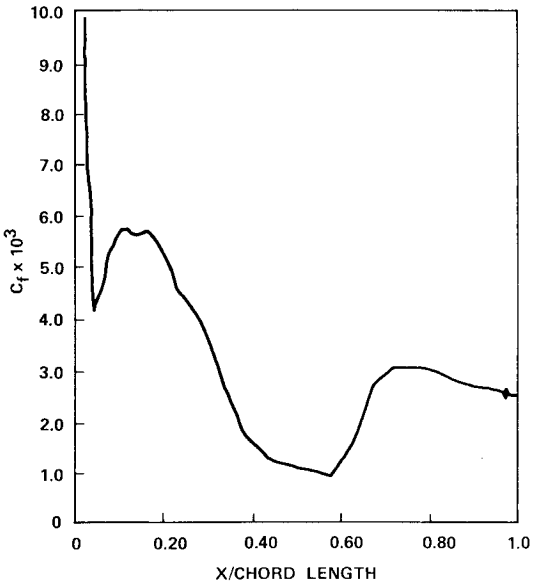

a) q-ω turbulence model

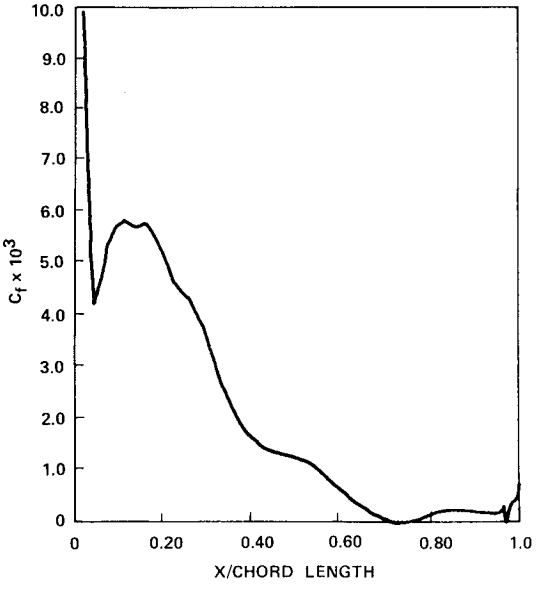

b) Laminar case

Fig. 11 Skin friction coefficient on E^3 vane suction surface.

deviation in loss predictions from experiment scales roughly as the square of the mesh spacing in the inviscid core region, as expected for a second-order accurate formulation. Extrapolation to zero mesh size implies a pressure loss of 1.2% for laminar flow and 2.4% for turbulent.

The deviation of loss predictions from experiment was established to be due to numerical error by integrating stagnation pressure over the inviscid core region only, where there should be no two-dimensional loss with irrotational incoming flow and negligible shock loss. This is illustrated in Fig. 12 for the refined grid, showing an absolute error in mass-average loss of about 0.3%. An explanation of the apparent discrepancy between this and the error estimate that follows from the extrapolation to zero mesh above is not available. Note also in Fig. 12 that most of the pressure loss occurs beyond 50–70% chord and across the trailing edge, with the dominant effect being base drag. Boundary layer transition has substantial impact on predicted loss.

Preliminary Three-Dimensional Results

The three-dimensional viscous cascade code, HCAS3D, was set up for linear cascades with a plane of symmetry at midspan. Coordinates are stored as 64-bit arrays to eliminate round-off error effects on the highly refined grids required for sublayer resolution. Also, metrics are evaluated using 64-bit arithmetic before storage in 32-bit arrays. Otherwise, HCAS3D is basically a single precision code. It has been applied to the Langston cascade and to the E^3 vane configuration with straight endwalls. Performance in both cases is good. In the interest of brevity and continuity of subject

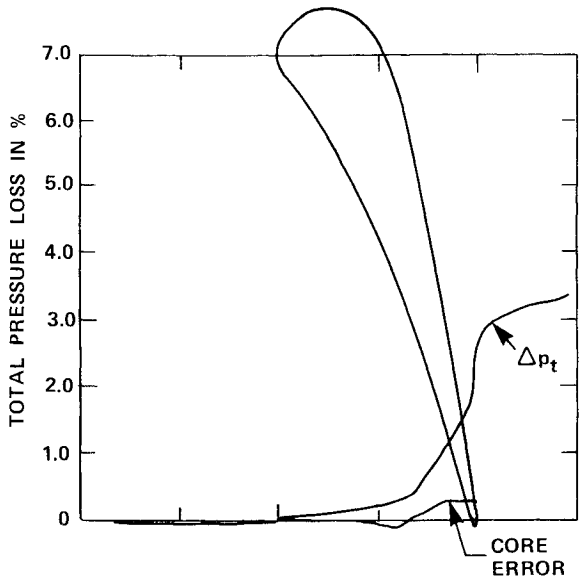

a) q-ω turbulence model

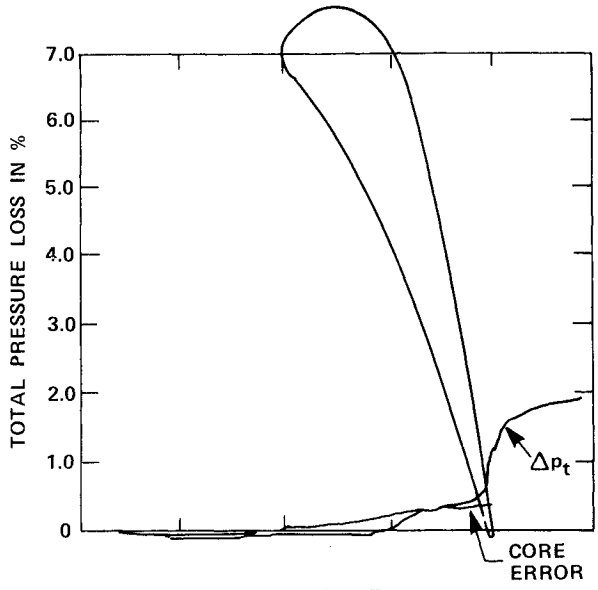

b) Laminar flow

Fig. 12 Axial variation of predicted pressure loss on 133 × 50 grid.

matter, only the latter results will be discussed here. The case considered[9,17] involves $M_e = 0.849$ and a Reynolds number of 6.41×10^5 based on exit properties and axial chordlength ($c_x = 3.34$ cm). The endwall boundary layer is specified at the inlet plane in accordance with experiment, using a power law profile exponent $n = 6.4$.

Sheared H-grid construction was altered for the three-dimensional computations as can be seen in Fig. 13, where every fourth gridline is plotted for clarity. Transverse gridlines converge from uniform spacing at the inflow and outflow planes to highly refined boundary-layer-type grids over the airfoil surface, starting at leading- and trailing-edge points. This considerably relieves convergence issues in the wake region. In addition, the downstream periodic gridline has been aligned with the mean exit flow angle at midspan. This was known from experiment as well as prior flow computations, but extension to a simple adaptive grid procedure is also straightforward.

A quarter of a million grid points were used to assure accurate stagnation pressure loss prediction and resolution of vortical flow details. This consists of the same 131 × 66 grid system for each x-y plane and stacking in the spanwise direction at 30 nonuniformly spaced locations. The minimum grid spacing normalized with respect to axial chord was 5×10^{-4} at the endwall and normal to the airfoil surface, and the maximum grid spacing was $0.05c_x$ in both transverse directions. The axial grid distribution is essentially unchanged from that for refined two-dimensional results. We had facility to handle this relatively large problem in core on our Alliant FX/8 computer. About 22 Mbyte of memory was required including FORTRAN code.

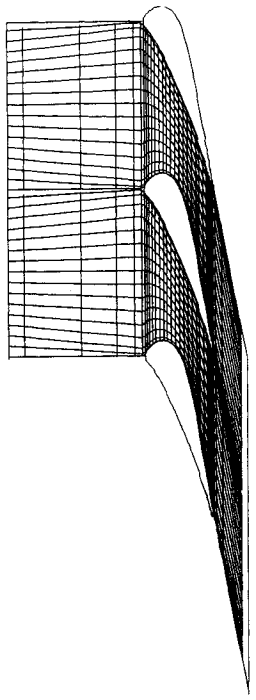

Fig. 13 Revised grid construction in each x-y plane used in three-dimensional computation.

Very complex flow phenomenology arises in a three-dimensional cascade passage, with considerable variation in spatial scale. This is illustrated by the development of the endwall velocity profile shown in Fig. 14 along the midline between vanes. Flow enters in the x direction at about Mach 0.1 with a thick endwall boundary layer as in the experiment. The same turbulent velocity profile is used at the inflow plane for both laminar and turbulent computations to give the same inflow vorticity and hence similar horseshoe vortex formation. Results in Fig. 14 are for the q-ω model. The boundary layer contracts due to rapid acceleration and then essentially restarts at the separation line along the track of the horseshoe vortex from saddle point to suction surface. Note the rapid development of a strong secondary flow component that is concentrated close to the endwall. A substantial wake region is evident downstream and the boundary layer is very thin. Fertile opportunity for adaptive grid procedures is evident. Secondary flow gradually decreases after the vane trailing edge, and flow exits at about Mach 0.8 after turning 79 deg through the cascade.

Predicted axial variation in mass-average total pressure loss for laminar and turbulent simulations are given in Fig. 15. The experimental data point measured 1 cm downstream of the trailing edge also is shown for comparison, including the estimated error bar. Prime contributors to loss are compared at that location in Table 3. Base drag due to the blunt trailing edge is included in profile loss and represents a major effect, as can be seen in Fig. 15. Agreement of the q-ω model with experiment is fair. Note that secondary flow loss is considerably underpredicted if laminar flow is assumed. Figure 16 shows loss contours at the experimental exit plane. Wake development proceeds more slowly for laminar flow, as would be expected. Flow structure details given by the q-ω model are

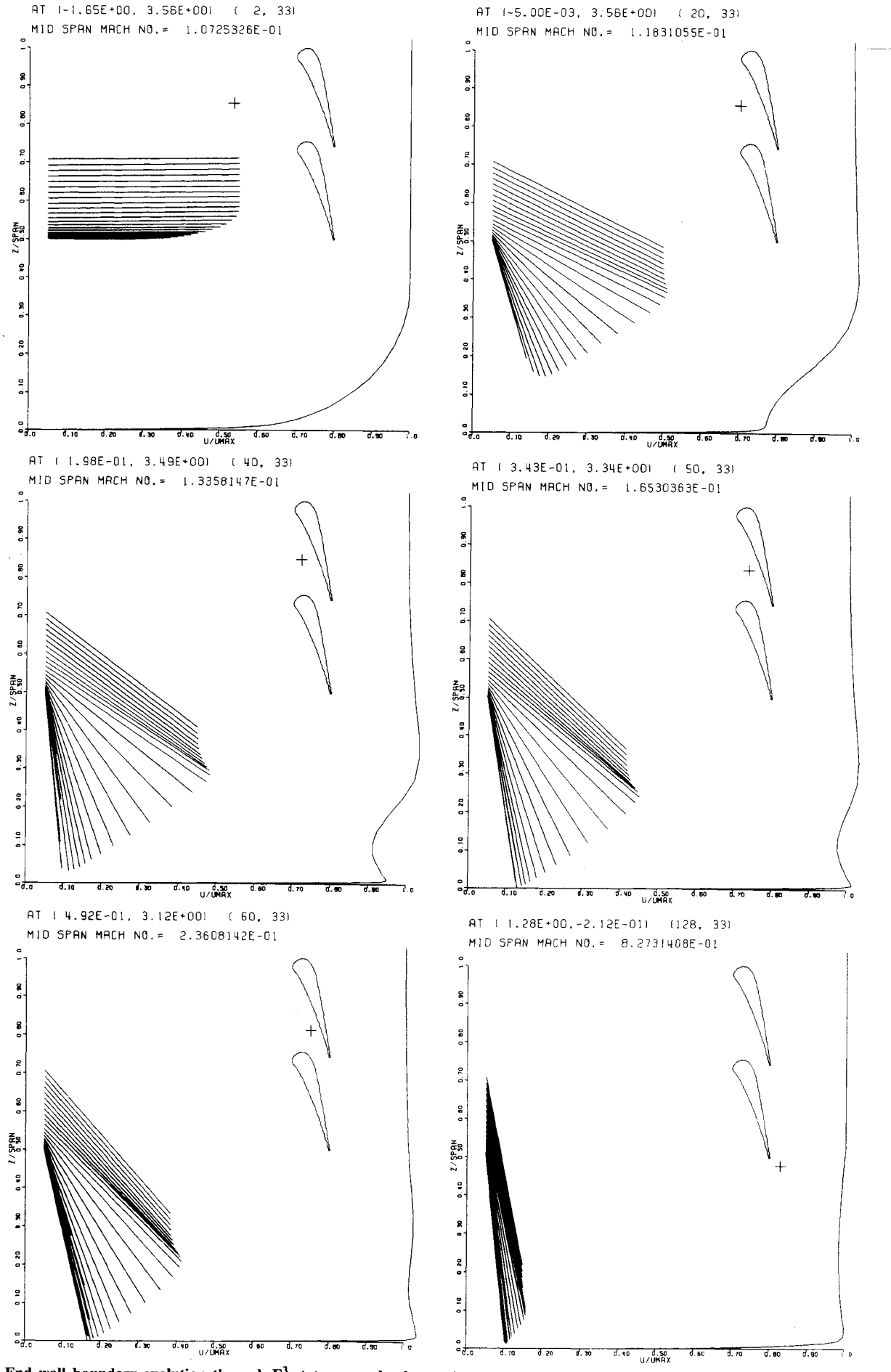

Fig. 14 End wall boundary evolution through E^3 stator cascade along midline between vanes (total velocity profile and flow angle given vs spanwise position for location indicated in blade passage).

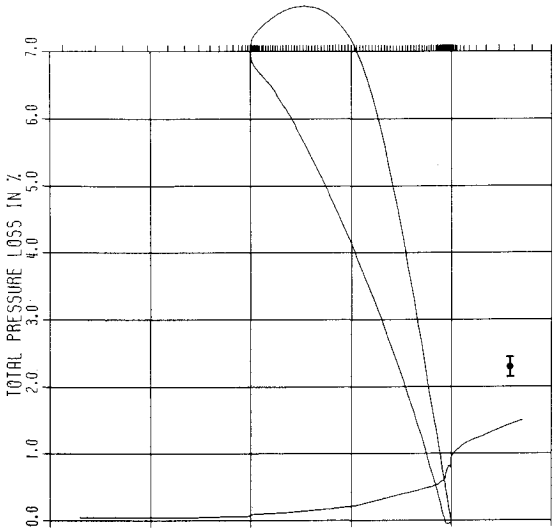

a) Laminar flow

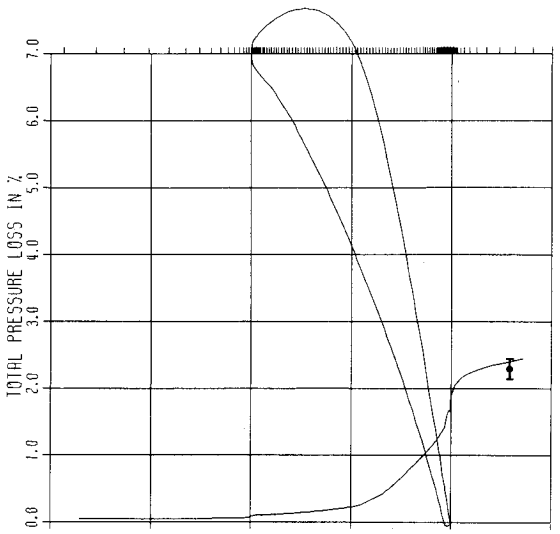

b) q-ω turbulence model

Fig. 15 Three-dimensional mass-average loss predictions for E³ vane at $M_e = 0.84$ (experimental data point from Ref. 9).

Table 3 Comparison of three-dimensional loss predictions for E³ stator to experiment at design point

	Experiment	Computation	
Loss	NASA CR-165567	Laminar	Turbulent
Profile	0.011	0.011	0.016
Secondary	0.013	0.004	0.008
Total	0.023	0.015	0.024

in good agreement with experiment.

The spanwise distributions of mass-average total pressure loss and exit flow angle are compared with experimental data in Figs. 17 and 18, respectively. Note that the passage vortex location is well predicted by the q-ω model, including underturning toward the midspan side and overturning near the wall. The endwall boundary layer thickness 1 cm downstream of the vane trailing edge is also roughly correct. There is asymmetry in experimental measurements of loss, also evident in Fig. 16. This may be due to different surface roughness on the two endwalls, which were made of different materials. Comparison of computational results to data on the lower endwall should be most relevant.

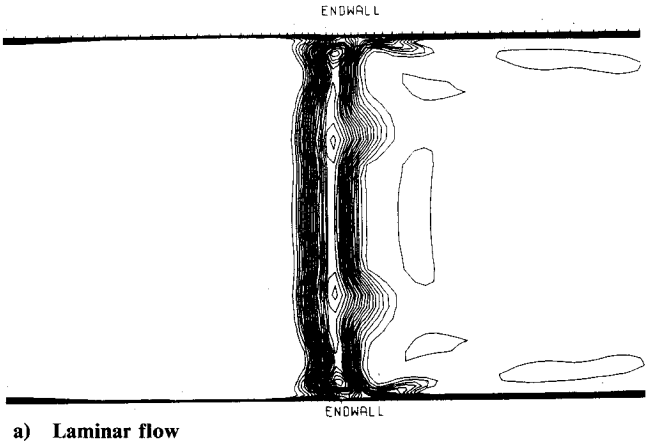

a) Laminar flow

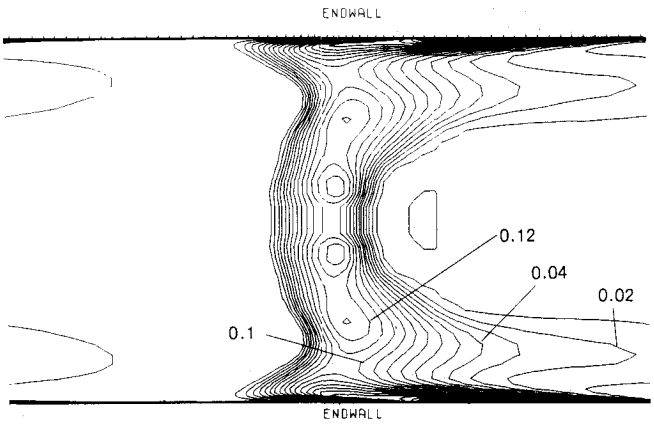

b) q-ω turbulence model

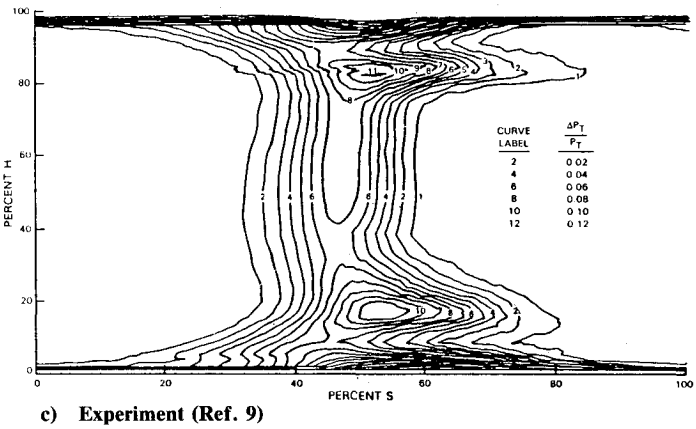

c) Experiment (Ref. 9)

Fig. 16 Stagnation pressure contours at exit plane ($x/c_x = 0.328$).

Conclusion

Viscous flow codes have been developed for two- and three-dimensional linear cascades based on scalar implicit approximate factorization and a special form of the thin layer approximation. These have been exercised assuming laminar as well as turbulent flow in order to better assess performance of the q-ω model, particularly with regard to predicting boundary layer transition. The latter capability has been only qualitatively assessed and not for intense freestream turbulence at this preliminary stage. Computational results on H-grids have been compared to experiment with good agreement. Considering the complexity of the flowfields involved, that is a very significant achievement.

Another key consideration is computational efficiency. Performance in that regard can be illustrated by considering the

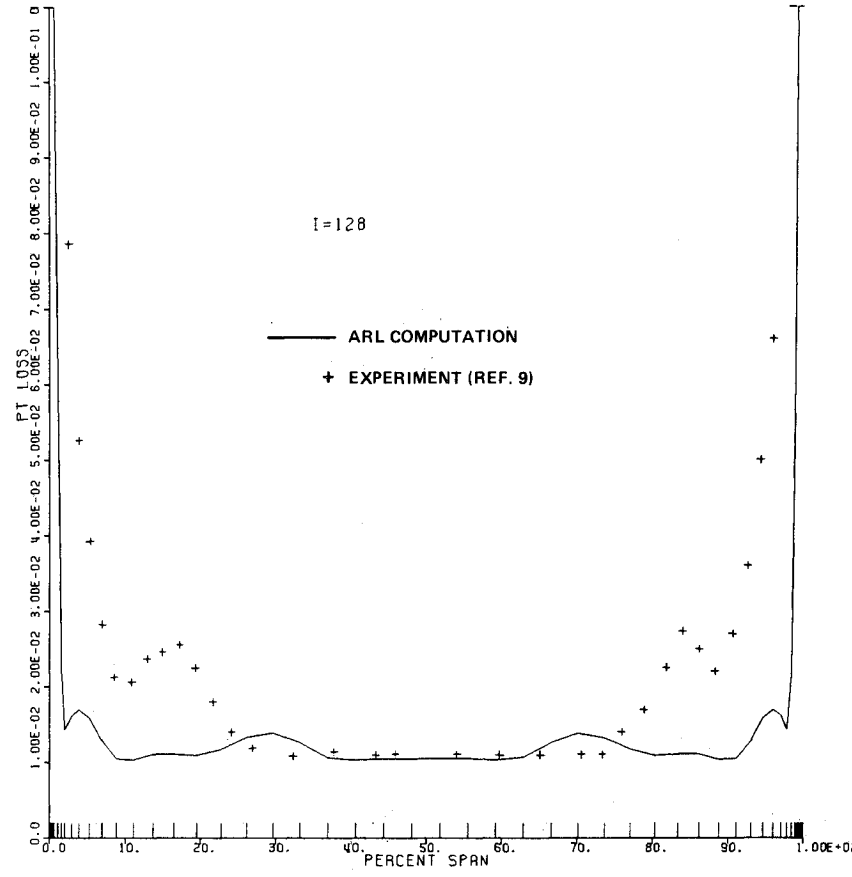

a) Laminar flow

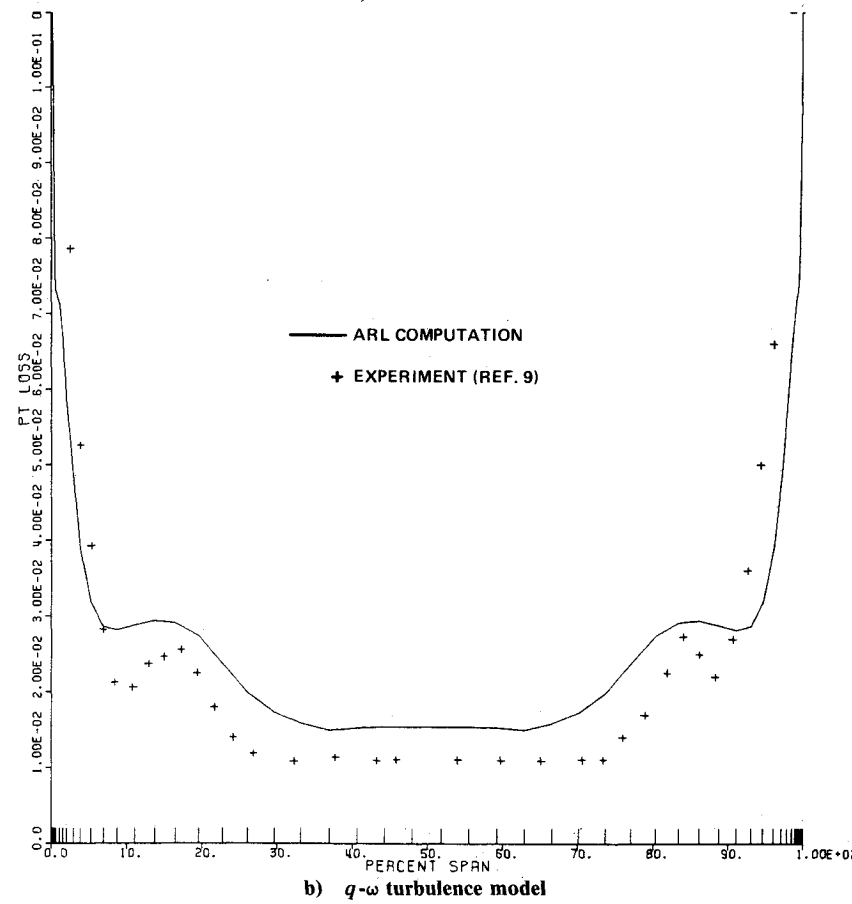

b) q-ω turbulence model

Fig. 17 Spanwise variation of mass-average loss at exit.

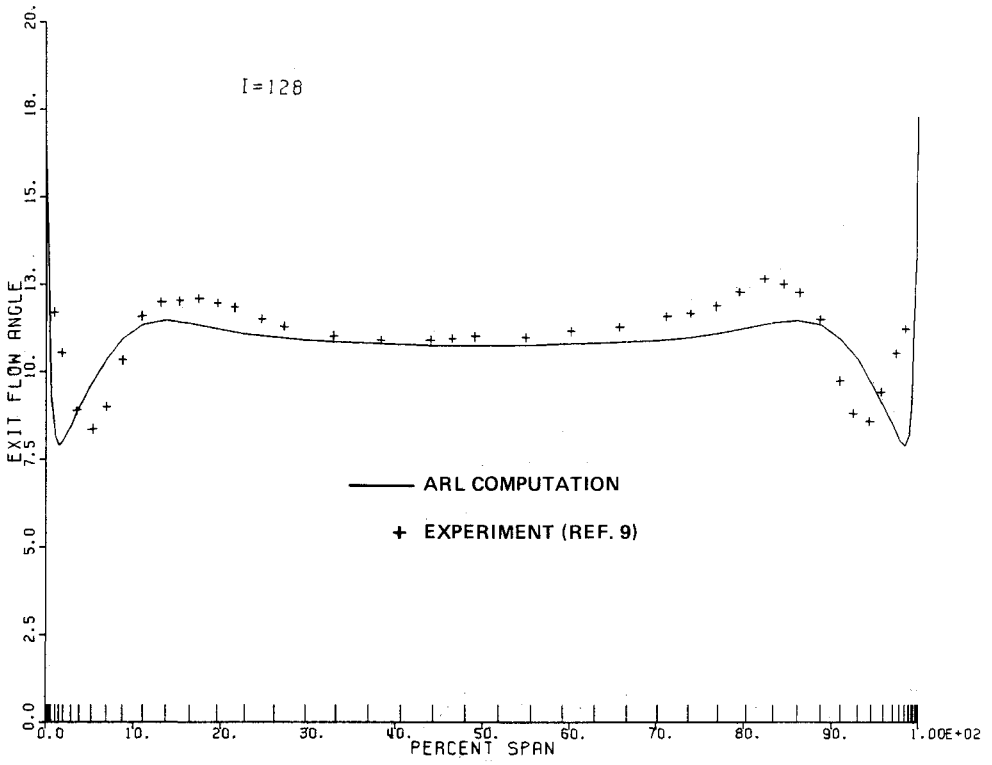

a) Laminar flow

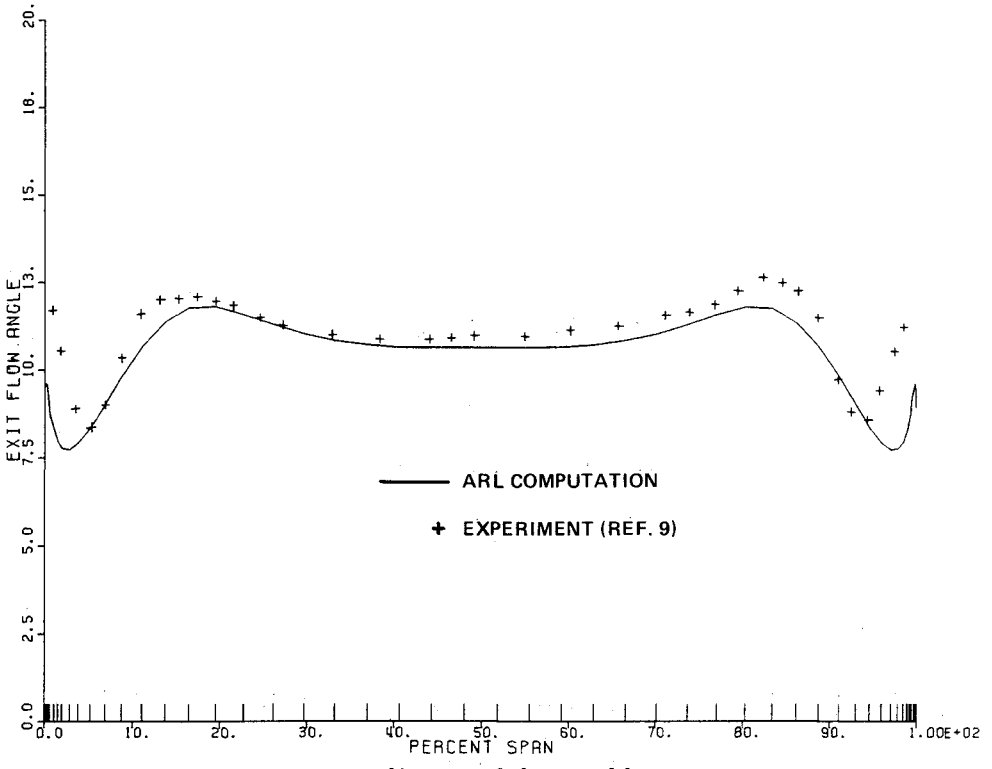

b) q-ω turbulence model

Fig. 18 Spanwise variation of mass-average flow angle at exit.

three-dimensional vane calculation on a $131 \times 66 \times 30$ grid. Code execution time is about 2.8×10^{-4} s/grid point/time step on an Alliant FX/8 with four computing elements. This is a multiprocessor and good hardware-supported concurrency has been achieved with code restructuring. Simultaneous vectorization of the code is still in process. Roughly 800 time steps are required for convergence with the q-ω model on a grid that resolves the viscous sublayer down to $y_+ \sim 1$. Timing estimates on an IBM 3090-200 scalar machine indicate 3.0×10^{-4} s/grid point/time step. This time is essentially the same as for a good explicit Runge-Kutta code for viscous annular cascades.[18] Recognizing the added cost associated with a scalar implicit scheme, a two-equation turbulence model vs Baldwin-Lomax, and second order upwinding as compared to central differencing plus damping, computational efficiency of the HCAS3D code is viewed as excellent.

Acknowledgment

This research was conducted under sponsorship of the Avco Lycoming Independent Research and Development (IRAD) Program. The authors wish to thank the Avco Lycoming/Textron management for financial support and permission to present these results.

References

[1]Pulliam, T. H. and Chausee, D. S., "A Diagonal Form of an Implicit Approximate-Factorization Algorithm," *Journal of Computational Physics,* Vol. 39, Feb. 1981, pp. 347–363.

[2]Coakley, T. J., "Numerical Method for Gas Dynamics Combining Characteristic and Conservation Concepts," AIAA Paper 81-1257, June 1981.

[3]Coakley, T. J., "Implicit Upwind Methods for the Compressible Navier-Stokes Equations," AIAA Paper 83-1958, July 1983.

[4]Pulliam, T. H. and Steger, J. L., "Recent Improvements in Efficiency, Accuracy, and Convergence for Implicit Approximate Factorization Algorithms," AIAA Paper 85-0360, Jan. 1985.

[5]Goldberg, U. and Reshotko, E., "Scaling and Modeling of Three-Dimensional, Pressure-Driven, Turbulent Boundary Layers," AIAA Paper 83-1695, July 1983.

[6]Horstman, C. C., "A Computational Study of Complex Three-Dimensional Compressible Turbulent Flowfields," AIAA Paper 84-1556, June 1984.

[7]Eibeck, P. A. and Eaton, J. K., "An Experimental Investigation of the Heat Transfer Effects of a Longitudinal Vortex Embedded in a Turbulent Boundary Layer," Thermo. Div. Dept. of Mechanical Engineering, Stanford Univ., Stanford, CA, Rept. MD-48, 1985.

[8]Rodi, W. and Scheurer, G., "Calculation of Heat Transfer to Convection-Cooled Gas Turbine Blades," *Journal of Engineering for Gas Turbines and Power,* Vol. 107, July 1985, pp. 620–627.

[9]Kopper, F. C., Milano, R., Davis, R. L., Dring, R. P., and Stoeffler, R. C., "EEE Component Development and Integration Program, High-Pressure Turbine Supersonic Cascade Technology Report," NASA CR-165567, Nov. 1981.

[10]Coakley, T. J., "Turbulence Modeling Methods for the Compressible Navier-Stokes Equations," AIAA Paper 83-1693, July 1983.

[11]Norton, R. J. G., Thompkins, W. T., and Haimes, R., "Implicit Finite Difference Schemes with Non-Simply Connected Grids—A Novel Approach," AIAA Paper 84-0003, Jan. 1984.

[12]Roe, P. L., "Approximate Riemann Solvers, Parameter Vectors, and Difference Schemes," *Journal of Computational Physics,* Vol. 43, Oct. 1981, pp. 357–372.

[13]Viegas, J., Private communication, May 1986.

[14]Cebeci, T. and Smith, A. M. O., *Analysis of Turbulent Boundary Layers,* Academic, New York, 1974, Chap. 6.

[15]Ramaprian, B. R., Patel, V. C., and Sastry, M. S., "Turbulent Wake Development behind Streamlined Bodies," Iowa Institute of Hydraulic Research, Univ. of Iowa, Iowa City, IIHR Rept. 231, July 1981.

[16]Marvin, J. G., "Turbulence Modeling for Computational Aerodynamics," *AIAA Journal,* Vol. 21, July 1983, pp. 941–955.

[17]Kopper, F. C., Milano, R., and Vanco, M., "Experimental Investigation of Endwall Profiling in a Turbine Vane Cascade," *AIAA Journal,* Vol. 19, Aug. 1981, pp. 1033–1040.

[18]Subramanian, S. V. and Bozzola, R., "Numerical Simulation of Three-Dimensional Flowfields in Turbomachinery Blade Rows using the Compressible Navier-Stokes Equations," AIAA Paper 87-1314, June 1987.